**Originally published as:**

Li, Q., Schultz, P., Lin, W., Kurths, J., Ji, P. (2020): Global and local performance metric with inertia effects. - Nonlinear Dynamics, 102, 2, 653-665.

# Global and local performance metric with inertia effects

Qiang Li[1,2,3], Paul Schultz[4], Wei Lin[1,2,3], Jürgen Kurths[4,5,6], and Peng Ji[1,2,3*]

[1]*Institute of Science and Technology for Brain-Inspired Intelligence, Fudan University, Shanghai 200433, China*

[2]*LCNBI and LMNS (Fudan University), Ministry of Education, Shanghai 200433, China*

[3]*Research Institute of Intelligent and Complex Systems, Fudan University, Shanghai 200433, China*

[4]*Potsdam Institute for Climate Impact Research (PIK), 14473 Potsdam, Germany*

[5]*Department of Physics, Humboldt University, 12489 Berlin, Germany*

[6]*Institute for Complex Systems and Mathematical Biology,*
*University of Aberdeen, Aberdeen AB24 3UE, United Kingdom*

A complex system's structural-dynamical interplay plays a profound role in determining its collective behavior. Irregular behavior in the form of macroscopic chaos, for instance, can be potentially exhibited by the Kuramoto model of coupled phase oscillators at intermediate coupling strength with frequency assortativity and this behavior is theoretically interesting. In practice, however, such irregular behavior is often not under control and is undesired for the system's functioning. How the underlying structural and oscillators' dynamical interplay affects a collective phenomenon (and its corresponding stability) after being subjected to disturbances, attracts great attention. Here, we exploit the concept of a coherency performance metric, as a sum of phase differences and frequency displacements, to evaluate the response to perturbations on network-coupled oscillators. We derive the performance metric as a quadratic form of the eigenvalues and eigenmodes corresponding to the unperturbed system and the perturbation vector, and analyze the influences of perturbation direction as well as strength on the metric. We further apply a computational approach to obtain the performance metric's derivative with respect to the oscillators' inertia. We finally extend the metric to a local definition which reflects the pairwise casual effects between any two oscillators. These results deepen the understanding of the combined effects of the structural (eigenmodes) and dynamical (inertia) effects on the system stability.

## I. Introduction

Complex networks play a vital role in revealing a hierarchical architecture of complex systems. Each element of a system exhibits its own dynamics determined by intrinsic governing equations and parameters. Once adjacency elements are coupled, the dynamics on the network induces the emergence of self-organization and other collective phenomena [1–3]. The induced phenomena, e.g. phase synchronization and chaos, are generally governed by the complex interplay between the intrinsic dynamics, the underlying network topology and the coupling strength. Though initially unexpected, coupled periodic systems were found to exhibit a chaotic regime over large portions of the parameter space, e.g. the paradigmatic Kuramoto model of coupled phase oscillators and its extensions [4]. On the one hand, different features are known to cause chaotic macroscopic dynamics. Such features might be preferential connections between oscillators with similar or dissimilar natural frequencies [5] or a time-varying coupling strength [6]. On the other hand, the Kuramoto model exhibits chaotic behavior at intermediate coupling strengths with positive Lyapunov exponents [7] or chaotic dynamic of order parameters [7, 8]. The chaotic behaviour, an essential property of the incoherent regime, is predominantly observed in systems of intermedite size and its corresponding hyper-chaotic regime vanishes in the infinite-size limit [8–10]. Additional to chaotic behavior, phase synchronization has been widely studied, from the aspects of the effects of inertia, the sufficient conditions to guarantee the phase synchronization, and

---

so on [11–15]. Even any non-zero inertia can induce the first-order phase transition from incoherence to coherence [16, 17]. The interplay between dynamical and structural properties leads to further various phenomena, including solitary states [18]. The induced phenomena can be further affected by phase shift [19] and time-delay feedback control [20], and should be explicitly taken into account the future design of power grids [19, 20].

In general, a dynamical system is unavoidable to be affected by internal and external perturbations [21, 22], where large perturbations in multistable settings might even lead to transitions to alternative attractors [23]. A central question arises of how to quantify the effects of perturbations on a system's long-term stability as well as how to characterise the transient behaviour. Various stability measures along the line of this research have been proposed, e.g., the master stability formalism given small perturbations [24]. For large perturbations, basin stability quantifies the probability of the system returning to a desired synchronous regime [25]. Commonly, these stable stationary states are characterized by phase coherency order parameters (see [26] for an overview). A further method to quantify the degree of synchronisation is the synchrony alignment function [27], capturing the interplay of the network topology and the spatial allocation of natural frequencies. However, to compare system transients following impulsive one-time perturbations, various observables have been tailored to different aspects of the time evolution. Commonly, a notion of return time measurement is employed, examples are synchronisation speed [28], relaxation rate [29] or finite-time basin stability [30]. Another approach is to construct energy-like functionals, e.g. quadratic performance metrics like coherency [31] or fragility measures [32], quantifying a respective kind of effort to regain synchronisation. These energy-like functionals characterize a global system stability, and local ones reflect causal effects between components, e.g. local response functions in Fourier space [33]. Additionally, to measure e.g. chaotic dynamics of the order parameter, as discussed above, quadratic performance metrics [7, 34] can be applied. Recently, it has been shown that the presence of (high) inertia is a distinctive ingredient to the emergence of chaotic dynamics in the form of intermittently chaotic transients and stable chaotic two-population states [35]. However, chaotic attractors as well as transients are often undesired for proper functioning of complex systems and the dynamics needs to be designed or controlled in a way to suppress chaos in favour of phase synchronisation.

Based on the previous work on performance metrics in this context (i.e. [31–33]), in this manuscript we further investigate a gradient formula for local quadratic performance metrics, extend the global approaches analytically derived in a strong coupling regime to a weak one and investigate the local approaches systematically. In particular, we focus on the Kuramoto model with inertia, mainly from perspectives of its theoretical interest (its evidence to chaotic dynamics) as well due to its widespread applications (especially to power transmission grids at a macroscopic scale [36]). In particular, we exploit the concept of performance metrics to investigate the Kuramoto model with inertia, and obtain its solution as a function of the spectral decomposition of the underlying network. We conduct a computational approach based on a gradient formula [31] and calculate its sensitivity with respect to the inertia. We analytically derive a local performance metric in the strong-coupling regime and finally validate the conclusions numerically in the weak-coupling regime.

## II. Model and coherency performance metric

Consider a network given by a graph $\mathcal{G} = (\mathcal{V}, \mathcal{E})$ with $N$ nodes $\mathcal{V} = \{1, \cdots, N\}$ and $M$ edges $\mathcal{E} \subseteq \mathcal{V} \times \mathcal{V}$. The adjacency matrix $\mathbf{A}$ of $\mathcal{G}$ with elements $a_{ij}$ quantifies the connection between nodes $i$ and $j$, with $a_{ij} = 1$ if $(i, j) \in \mathcal{E}$ and $a_{ij} = 0$ otherwise. Each node of the network is governed by the second-order Kuramoto dynamics as follows

$$\dot{\theta}_i = \omega_i,$$
$$\dot{\omega}_i = -\frac{1}{m_i}\omega_i + \frac{P_i}{m_i} - \frac{K}{m_i}\sum_{j=1}^{N} a_{ij}\sin(\theta_i - \theta_j), \tag{1}$$

where the state of the $i$-th node consists of its phase $\theta_i$ and frequency $\omega_i$, $m_i \geq 0$ denotes the inertia, $P_i$ the power and $K$ is the coupling strength. We consider the network $\mathcal{G}$ has $N_1$ consumers (with $P_i<0$) and $N_2$ generators (with $P_i>0$), the sum of $P_i$ satisfies $\sum_{i=1}^{N} P_i = 0$. To simplify the calculation further, we take $P_i = -\frac{1}{N_1}$ if the $i$-th node is consumer, and otherwise $P_i = \frac{1}{N_2}$. The classical Kuramoto order parameter $R$ measures the phase coherence of the stationary state and is defined as [26]

$$Re^{\mathrm{i}\psi} = \frac{1}{N} \sum_{j=1}^{N} e^{\mathrm{i}\theta_j}, \tag{2}$$

where $\psi$ is the average phase of the nodes and $\mathrm{i} = \sqrt{-1}$. With the increase of the coupling strength $K$, the system undergoes a phase transition from incoherent to coherent states in the macroscopic dynamics. With small $K$ and the phases are uniformly distributed on the interval $[0; 2\pi]$, we have $R \approx 0$ and there is no macroscopic rhythm. In a range of intermediate $K$, irregular interesting behavior of chaotic dynamics could occur, especially when nodes prefer connecting with similar (dissimilar) frequency to each other [5]. As illustrated in Fig. 1, we show that for weak-coupling strengths, the second-order Kuramoto model could exhibit chaotic dynamics with positive maximum Lyapunov exponent and the chaotic order parameter in macroscopic scale. In Fig. 1(a), black dots denote different realizations and the red line indicates the mean value. Figure 1(b) shows one realization of the order parameter $R$ with the mean value (the red-dot line) and the standard deviation (the shaded area). In the strong coupling regime, the mutual phase differences become small and all phases form a coherent group such that $R \approx 1$. The interplay between dynamical properties between nodes, e.g., frequency assortativity, is crucial to system dynamics. Assume that the system is initially located in the regime of a stationary phase synchronized state denoted as $\theta_i^{(0)}$ and $\omega_i^{(0)}$. Denoting $\boldsymbol{\theta} = [\theta_1, \cdots, \theta_N]$ and $\boldsymbol{\omega} = [\omega_1, \cdots, \omega_N]$, we focus on the system's response to perturbations to the stationary state and define difference coordinates as

$$\delta\boldsymbol{\theta}(t) = \boldsymbol{\theta}(t) - \boldsymbol{\theta}^{(0)} \text{ and } \delta\boldsymbol{\omega}(t) = \boldsymbol{\omega}(t) - \boldsymbol{\omega}^{(0)}. \tag{3}$$

We consider small perturbations with normal distribution and linearize the system (1) at the stationary state. This yields

$$\begin{bmatrix} \delta\dot{\boldsymbol{\theta}} \\ \delta\dot{\boldsymbol{\omega}} \end{bmatrix} = \begin{bmatrix} \mathbf{0} & \mathbf{I} \\ -K\mathbf{M}^{-1}\mathbf{L} & -\mathbf{M}^{-1} \end{bmatrix} \begin{bmatrix} \delta\boldsymbol{\theta} \\ \delta\boldsymbol{\omega} \end{bmatrix} + \begin{bmatrix} \mathbf{I} & \mathbf{0} \\ \mathbf{0} & \mathbf{M}^{-1} \end{bmatrix} \delta\mathbf{P} \, \delta(t), \tag{4}$$

where $\mathbf{I}$ is the identity matrix, $\mathbf{M} = diag\{m_i\}$ is the inertia matrix, and $diag\{m_i\}$ is a diagonal matrix $\mathbf{M}$ with elements $\mathbf{M}_{ii} = m_i$. $\mathbf{L}$ is the weighted Laplacian matrix with diagonal elements $\mathbf{L}_{ii} = \sum_{j=1}^{N} a_{ij}\cos(\theta_i^{(0)} - \theta_j^{(0)})$ and off-diagonal elements $\mathbf{L}_{ij} = -a_{ij}\cos(\theta_i^{(0)} - \theta_j^{(0)})$. $\delta(t)$ is the Dirac delta function, which is zero except at $t = 0$,

$$\delta(t) = \begin{cases} +\infty, & t = 0, \\ 0, & t \neq 0, \end{cases} \tag{5}$$

and satisfies the identity $\int_{-\infty}^{+\infty} \delta(t)dt = 1$ [37]. Here, $\delta\mathbf{P}$ is the perturbation vector

$$\delta\mathbf{P} = \begin{bmatrix} \boldsymbol{v}^\theta \\ \boldsymbol{v}^\omega \end{bmatrix} \in \mathbb{R}^{2N}, \tag{6}$$

where both the amplitude and the location of the perturbations are characterized in two random constants $\boldsymbol{v}^\theta \in \mathbb{R}^N$ and $\boldsymbol{v}^\omega \in \mathbb{R}^N$. $\delta\mathbf{P} \, \delta(t)$ implies that the perturbations are instantaneous at $t = 0$ and disappear at $t > 0$. In what follows, we perturb the phase $\theta_q$ and frequency $\omega_q$ of the $q$-th node with an impulse at t=0, with $v_i^\theta \neq 0$ and $v_i^\omega \neq 0$ if
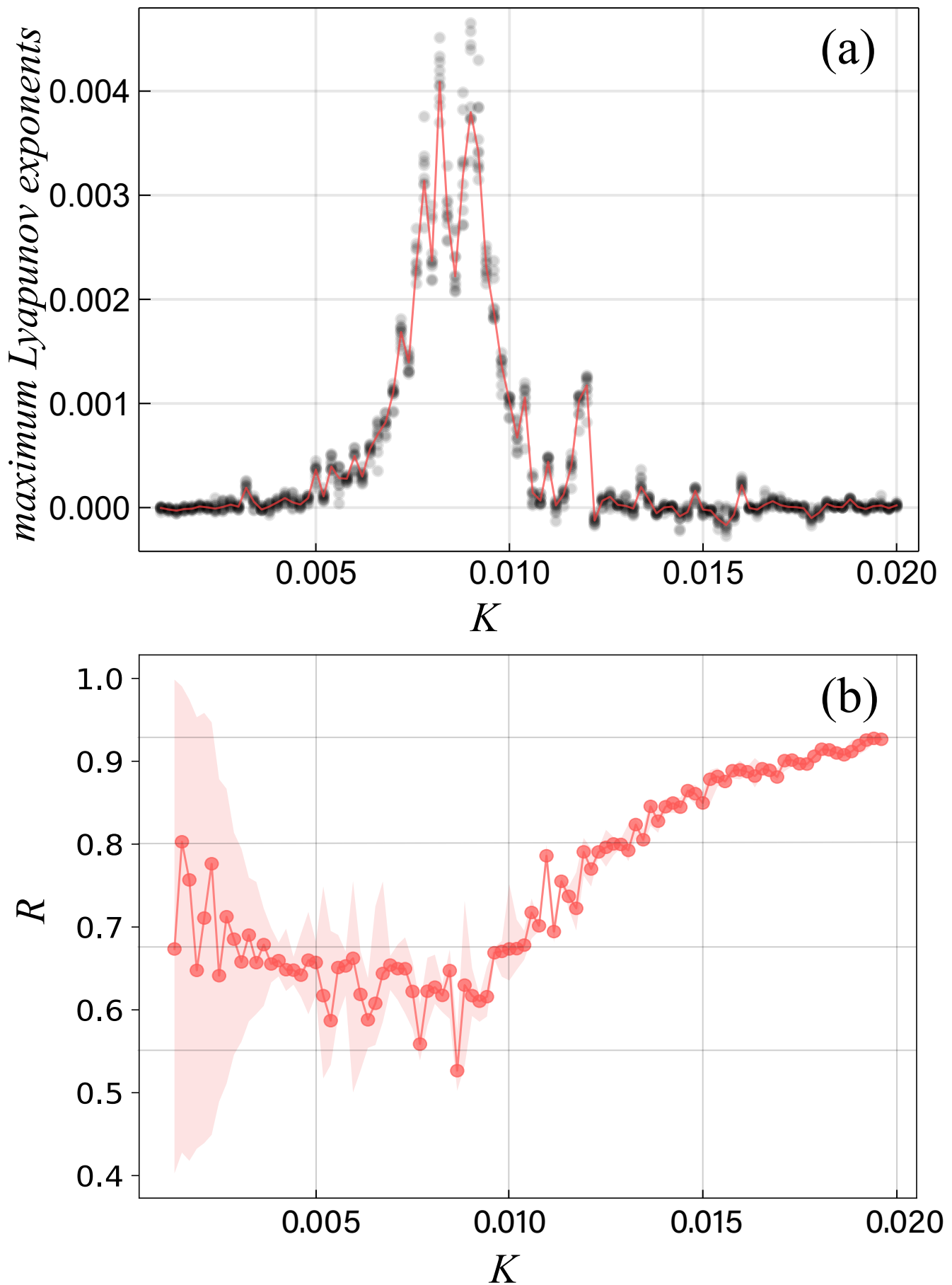
FIG. 1: Illustration of the emergence of chaos. In the weak-coupling regime, the system (1) can exhibit chaotic dynamics, which can be quantified by the maximum Lyapunov exponents (a) and represented by the order parameter in macroscopic scale (b). In (a), black dots denote different realizations and the red line indicates the mean value. (b) shows one realization of the order parameter $R$ with the mean value (the red-dot line) and the standard deviation (the shaded area). For the calculation of Lyapunov exponents, we use *ChaosTools* from the Julia library. Here, we take an Erdős-Rényi graph with $N = 100$ nodes and the connection probability equal to $p = 0.05$, $m_i = 1$, $N_1 = 30$, $N_2 = 70$, and $K$ varies within the range of $[0, 0.02]$.

$i = q$; $v_i^\theta = 0$ and $v_i^\omega = 0$ otherwise. Substituting Eq. (6) into Eq. (4), we obtain the following solution of the overall linear system

$$\dot{\mathbf{x}} = \mathbf{J}\mathbf{x} + \mathbf{B}\ \delta\mathbf{P}\ \delta(t). \tag{7}$$

**Lemma 1** (Solution for the linear system). *With the initial condition* $\mathbf{x}(0) = \mathbf{0}$, *the solutions of Eq. (7) are*

$$\mathbf{x}(t) = e^{\mathbf{J}t}\mathbf{B}\delta\mathbf{P}. \tag{8}$$

*where*

$$\mathbf{J} = \begin{bmatrix} \mathbf{0} & \mathbf{I} \\ -K\mathbf{M}^{-1}\mathbf{L} & -\mathbf{M}^{-1} \end{bmatrix}, \quad \mathbf{x} = \begin{bmatrix} \delta\boldsymbol{\theta} \\ \delta\boldsymbol{\omega} \end{bmatrix} \textit{ and } \mathbf{B} = \begin{bmatrix} \mathbf{I} & \mathbf{0} \\ \mathbf{0} & \mathbf{M}^{-1} \end{bmatrix}.$$

*Proof.* We multiply Eq. (7) by an integrating factor $e^{-\mathbf{J}t}$, and rewrite Eq. (7) as

$$e^{-\mathbf{J}t}\dot{\mathbf{x}} - e^{-\mathbf{J}t}\mathbf{J}\mathbf{x} = e^{-\mathbf{J}t}\mathbf{B}\ \delta\mathbf{P}\ \delta(t). \tag{9}$$

Using the fact that $e^{-\mathbf{J}t}\dot{\mathbf{x}} - e^{-\mathbf{J}t}\mathbf{J}\mathbf{x} = \frac{d}{dt}(e^{-\mathbf{J}t}\mathbf{x})$, and integrating Eq. (9) from 0 to t, we obtain

$$e^{-\mathbf{J}t}\mathbf{x}(t) - \mathbf{x}(0) = \int_0^t e^{-\mathbf{J}\tau}\mathbf{B}\ \delta\mathbf{P}\ \delta(\tau)d\tau. \tag{10}$$

To solve the right side of Eq. (10), using $\int_0^t f(\tau)\delta(\tau)d\tau = f(0)$ for all reasonably well behaved function $f$ [38], we have

$$e^{-\mathbf{J}t}\mathbf{x}(t) - \mathbf{x}(0) = \mathbf{B}\delta\mathbf{P}. \tag{11}$$

Therefore, with the initial condition $\mathbf{x}(0) = \mathbf{0}$, we obtain the solutions of Eq. (7) as

$$\mathbf{x}(t) = e^{\mathbf{J}t}\mathbf{B}\delta\mathbf{P}. \tag{12}$$

$\square$

We can decompose Eq. (8) into eigenmodes of the system Eq. (7) by diagonalizing the Jacobian matrix $\mathbf{J}$, which admits a set of right eigenvectors $\{\mathbf{u}_1^r \cdots \mathbf{u}_{2N}^r\}$, and

$$\mathbf{J}\mathbf{u}_i^r = \lambda_i \mathbf{u}_i^r,$$

for $i = 1, \cdots, 2N$. We assume that the parameters of Eq. (1) are selected such that the origin is asymptotically stable. Then the eigenvalues $\lambda_i$ of $\mathbf{J}$ are complex-valued with $\mathrm{Re}(\lambda_i) < 0$ for $i = 2, \cdots, 2N$, where $\mathrm{Re}(\lambda_i)$ is the real part of $\lambda_i$, and $\lambda_1 = 0$ corresponding to a global phase shift symmetry. Typically, $\mathbf{J}$ is asymmetric and not diagonalized through a unitary transformation, i.e. it is not normal and the right and left eigenvectors are not identified with each other. The left eigenvectors are determined by $\mathbf{u}_i^{l\dagger}\mathbf{J} = \lambda_i \mathbf{u}_i^{l\dagger}$ where $\mathbf{u}_i^{l\dagger}$ is the conjugate transpose of $\mathbf{u}_i^l$. We can, however, form a biorthogonal basis by employing the condition $\langle \mathbf{u}_i^l, \mathbf{u}_j^r \rangle = \mathbf{u}_i^{l\dagger}\mathbf{u}_j^r = 1$ if $i = j$ and $\langle \mathbf{u}_i^l, \mathbf{u}_j^r \rangle = 0$ otherwise. We write an eigendecomposition of $\mathbf{J}$ as

$$\mathbf{J} = \sum_{i=2}^{2N} \lambda_i \mathbf{u}_i^r \mathbf{u}_i^{l\dagger}. \tag{13}$$
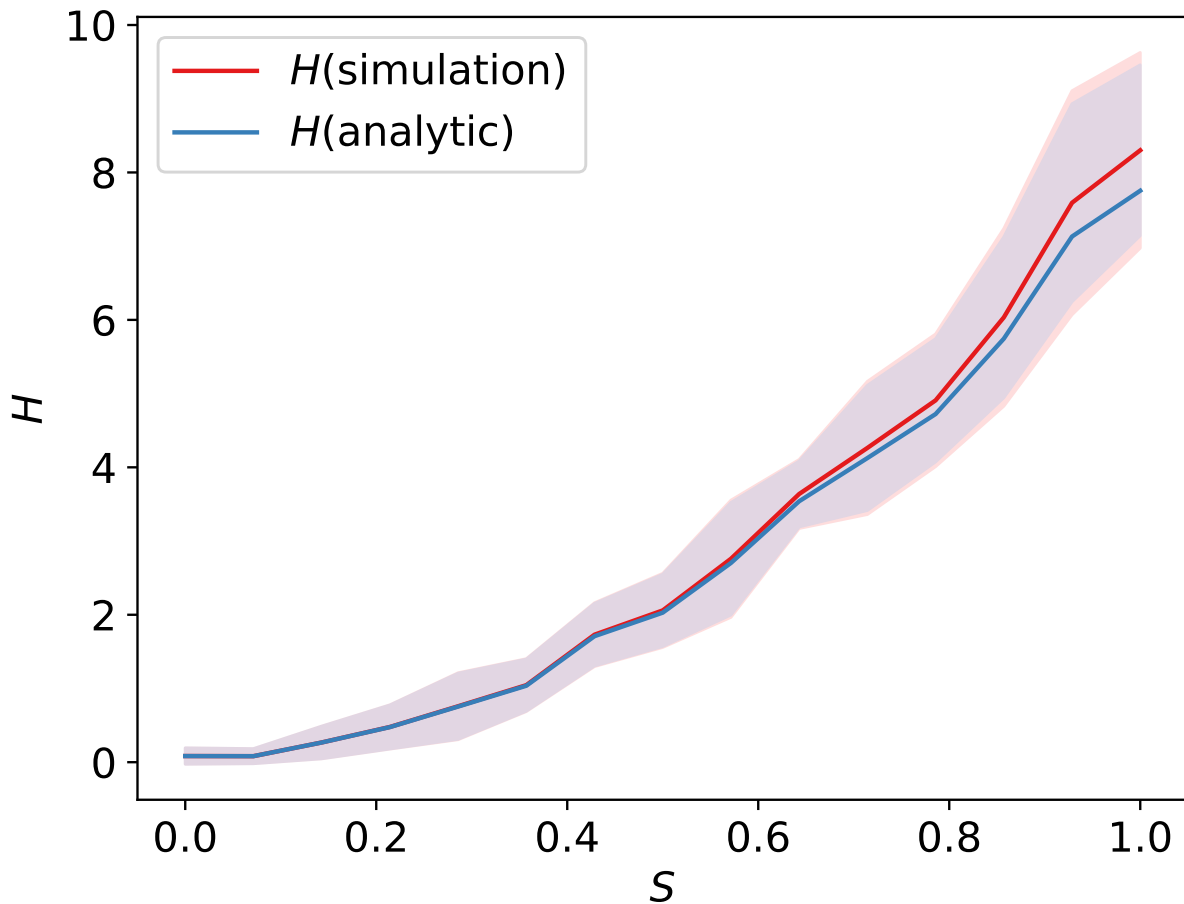
FIG. 2: Variations of analytic and simulation solutions of $H$ caused by perturbations $S$, where the perturbations are normally distributed with standard deviation 0.1 and mean $S$, and we take the coupling strength $K = 1.0$, the inertia $m_i = 1.0$, $N_1 = 30$, and $N_2 = 70$. The x-axis and the y-axis represent the mean $S$ and the solutions of $H$, respectively.

Substituting Eq. (13) into Eq. (8) results in the solution of $\mathbf{x}$ as

$$\mathbf{x}(t) = \sum_{i=2}^{2N} \mathbf{u}_i^r e^{\lambda_i t} \langle \mathbf{u}_i^l, \mathbf{B}\delta\mathbf{P} \rangle. \tag{14}$$

To compare the transient response to perturbations given by Eq. (6) in the linear regime, we exploit the quadratic coherency performance metric [31] as

$$H = \int_0^\infty \left\{ \sum_{i,j=1}^N a_{ij}(\delta\theta_i(t) - \delta\theta_j(t))^2 + \frac{1}{2}\sum_{i=1}^N m_i \delta\omega_i^2(t) \right\} dt. \tag{15}$$

$H$ sums the potential $H_p$ and the kinetic $H_k$ energy when the system returns to the stationary state, where the potential energy is defined as $H_p = \int_0^\infty \left\{ \sum_{i,j=1}^N a_{ij}(\delta\theta_i(t) - \delta\theta_j(t))^2 \right\} dt$ and the kinetic energy is defined as $H_k = \frac{1}{2}\int_0^\infty \left\{ \sum_{i=1}^N m_i \delta\omega_i^2(t) \right\} dt.$

**Lemma 2** (Coherency performance metric). *Using the the solution of* $\mathbf{x}$, *we rewrite* $H$ *as*

$$H = -\sum_{i,j=2}^{2N} \frac{1}{\lambda_i^* + \lambda_j} \langle \mathbf{B}\delta\mathbf{P}, \mathbf{u}_i^l \rangle \langle \mathbf{u}_j^l, \mathbf{B}\delta\mathbf{P} \rangle \langle \mathbf{u}_i^r, \mathbf{Q}\mathbf{u}_j^r \rangle, \tag{16}$$

*where*

$$\mathbf{Q} = \begin{bmatrix} 2\tilde{\mathbf{L}} & \mathbf{0} \\ \mathbf{0} & \frac{1}{2}\mathbf{M} \end{bmatrix}, \tag{17}$$

*and* $\lambda_i^*$ *is the complex conjugate of* $\lambda_i$ *and we omit* $\lambda_1 = 0$ *due to the orthogonality of the eigenvectors.*

*Proof.* We rewrite Eq. (15) as

$$H = \int_0^\infty \delta\boldsymbol{\theta}^\top \tilde{\mathbf{L}}\delta\boldsymbol{\theta} + \frac{1}{2}\delta\boldsymbol{\omega}^\top \mathbf{M}\delta\boldsymbol{\omega} dt, \tag{18}$$

where $\tilde{\mathbf{L}} \in \mathbb{R}^{N \times N}$ is the unweighted graph Laplacian matrix of the underlying network with the diagonal elements $\tilde{\mathbf{L}}_{ii} = \sum_{j=1}^N a_{ij}$ and the off-diagonal elements $\tilde{\mathbf{L}}_{ij} = -a_{ij}$. Here, $\tilde{\mathbf{L}}$ is different from $\mathbf{L}$ introduced in Eq. (4) due to the additional weights. For a sufficiently large coupling strength $K$, the system (1) could be located in a stationary state, and we therein have $\theta_i^{(0)} \approx \theta_j^{(0)}$ for $i, j = 1, \cdots, N$ and $\tilde{\mathbf{L}} \approx \mathbf{L}$. Now, using the definition of the state vector $\mathbf{x}$, $H$ can also be rewritten succinctly as

$$H = \int_0^\infty \mathbf{x}^\top \mathbf{Q}\mathbf{x} dt, \tag{19}$$

where

$$\mathbf{Q} = \begin{bmatrix} 2\tilde{\mathbf{L}} & \mathbf{0} \\ \mathbf{0} & \frac{1}{2}\mathbf{M} \end{bmatrix}. \tag{20}$$

Substituting Eq. (14) into Eq.(19) and using the fact that $\mathrm{Re}(\lambda_i) < 0$ for $i = 2, \cdots, 2N$ yields

$$H = \int_0^\infty dt\, e^{(\lambda_i^* + \lambda_j)t} \sum_{i,j=2}^{2N} \langle \mathbf{B}\delta\mathbf{P}, \mathbf{u}_i^l \rangle \langle \mathbf{u}_j^l, \mathbf{B}\delta\mathbf{P} \rangle \langle \mathbf{u}_i^r, \mathbf{Q}\mathbf{u}_j^r \rangle$$

$$= -\sum_{i,j=2}^{2N} \frac{1}{\lambda_i^* + \lambda_j} \langle \mathbf{B}\delta\mathbf{P}, \mathbf{u}_i^l \rangle \langle \mathbf{u}_j^l, \mathbf{B}\delta\mathbf{P} \rangle \langle \mathbf{u}_i^r, \mathbf{Q}\mathbf{u}_j^r \rangle. \tag{21}$$

$\square$

To validate the analytical expression Eq. (16) of the coherency performance metric, we apply Eq. (15) to numerical simulations of the nonlinear system. We consider an ensemble of Erdős-Rényi graphs with $N$ nodes and connection probability equal to $p = 0.05$. The perturbations are applied at $t = 0$ to a random selected node $q$ and follow a normal distribution with mean $S$ and standard deviation 0.1. Given $S$, two random values $v_q^\theta$ and $v_q^\omega$ are obtained from a uniform distribution, i.e. the phase and frequency of the $q$-th node are perturbed, respectively. The variations of the simulations and analytic solutions of $H$ with the magnitude of the perturbation vector are shown in Fig. 2. For small $S$ the numerical solutions of $H$ match well with the analytic solutions and confirm the validity of the linear approximation Eq. (7). Naturally, with $S$ increasing from 0 to 1, the differences between the analytic solutions and the simulation results also increase.
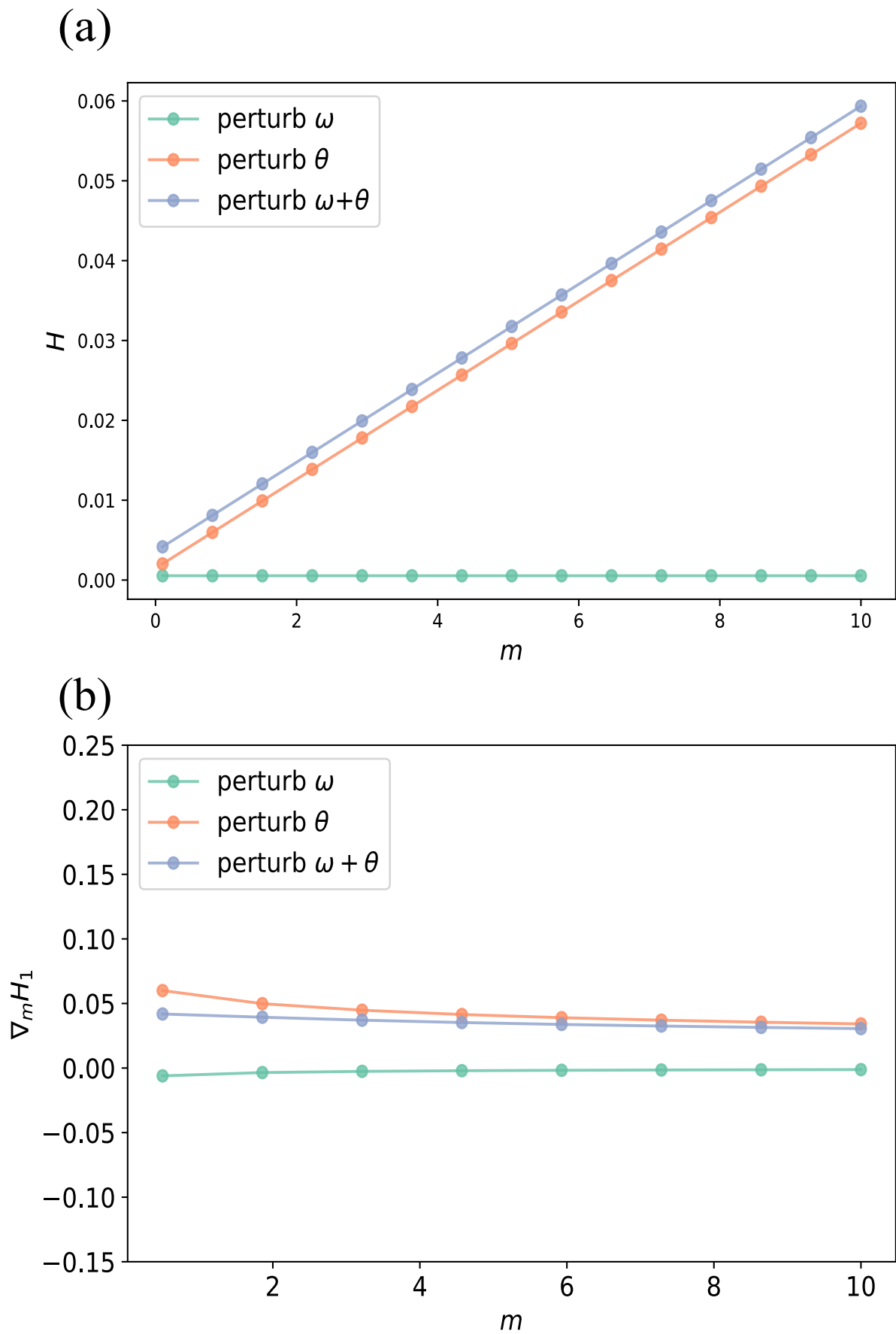
FIG. 3: (a) Coherency performance metric $H$ with respect to the inertia $m$, where $m$ is from 0.1 to 10, $K = 1.0$, and $q = 1$, i.e., we perturb the first node. The x-axis and the y-axis represent changes in $m$ and $H$, respectively. (b) $(\nabla_m H)_q$ with respect to the inertia $m$ for the three perturbation cases, where $m$ is from 0.5 to 10, $q = 1$, i.e., we perturb the first node. Here, $N_1 = 30$ and $N_2 = 70$. The x-axis and the y-axis represent changes in $m$ and $\nabla_m(H)_1$, respectively.

## III. Inertia effects

Besides external perturbations, Eq. (16) shows that the intrinsic inertia is another important factor for the coherency performance metric. To asses how $H$ itself depends on the local inertia, we systematically vary $m$ in the interval $[0.1; 10]$ following the configuration in Fig. 2. For simplicity, hereafter identical inertia constants are considered, i.e. $\mathbf{M} = m\mathbf{I}$ is a scalar matrix. Especially, we perturb the phase and/or the frequency locally at a randomly selected node $q$ in the following three cases: (i) perturb $\omega_q$, i.e. $v_q^\theta = 0$ and $v_q^\omega \neq 0$ in the vector $\delta\mathbf{P}$; (ii) perturb $\theta_q$, i.e. $v_q^\theta \neq 0$ and $v_q^\omega = 0$; (iii) perturb $\omega_q$ and $\theta_q$ simultaneously, i.e. $v_q^\theta \neq 0$ and $v_q^\omega \neq 0$. As shown in Fig. 3(a), for case (i), $H$ is independent of $m$, while for the cases (ii) and (iii), $H$ monotonically increases with respect to $m$ and inertia effects on the coherency performance metric are significant.

To support the numerical evidence in Fig. 3(a), we derive the sensitivity of $H$ to local inertia for the system Eq. (1) subject to small perturbations ($S \ll 1$). For this aim, we conduct a computational approach based on a gradient formula following the general framework of [31]. Concretely, we calculate the gradient $\nabla_m H$ of $H$ on the inertia and derive an algorithm for evaluating $\nabla_m H$. Substituting Eq. (8) into Eq. (19), we have

$$H = \delta\mathbf{P}^\top \mathbf{B}^\top \int_0^\infty e^{\mathbf{J}^\top t} \mathbf{Q} e^{\mathbf{J}t} dt \ \mathbf{B}\delta\mathbf{P}, \tag{22}$$

where $\mathbf{B}$, $\mathbf{J}$ and $\mathbf{Q}$ all depend on $m$. In this case, $H$ is a function of $m$, denoted by $H(m)$. To obtain the $\nabla_m H$, we show the Lemma 1 as follows.

**Lemma 3** (Derivative formula). *The directional derivative $D_{\boldsymbol{\xi}} H(m)$ along a unit vector $\boldsymbol{\xi} \in \mathbb{R}^N$ is defined as*

$$D_{\boldsymbol{\xi}} H(m) = \lim_{\sigma \to 0} \frac{H(m + \sigma\boldsymbol{\xi}) - H(m)}{\sigma}. \tag{23}$$

$H(m + \sigma\boldsymbol{\xi})$ *are considered as functions of a scalar $\sigma$ and are expanded in a Taylor series around $\sigma = 0$. $H^{(1)}(m, \boldsymbol{\xi})$ denotes the coefficient of $\sigma$, and we have*

$$D_{\boldsymbol{\xi}} H(m) = H^{(1)}(m, \boldsymbol{\xi}) \,. \tag{24}$$

*Proof.* For a sufficient small $\sigma$, the Taylor expansion of $H(m + \sigma\boldsymbol{\xi})$ is

$$H(m + \sigma\boldsymbol{\xi}) = H(m) + H^{(1)}(m, \boldsymbol{\xi})\sigma + O(\sigma^2). \tag{25}$$

Substituting Eq. (25) into Eq. (23), and using $\sigma \to 0$, we have

$$D_{\boldsymbol{\xi}} H(m) = H^{(1)}(m, \boldsymbol{\xi}) \,.$$

$\square$

In fact, the directional derivative $D_{\boldsymbol{\xi}} H(m)$ is the partial derivative of $H(m)$ along a selected direction $\boldsymbol{\xi} \in \mathbb{R}^N$. $\nabla_m H = [(\nabla_m H)_1, (\nabla_m H)_2, \cdots, (\nabla_m H)_N]^T$, where $(\nabla_m H)_q$ is the partial derivative of $H(m)$ along the $q$-th orthonormal basis $\boldsymbol{e}_q \in \mathbb{R}^N$. Consequently, we obtain $(\nabla_m H)_q$ by a special choice $\boldsymbol{\xi} = \boldsymbol{e}_q$ from $D_{\boldsymbol{\xi}} H(m)$, i.e.,

$$(\nabla_m H)_q = D_{\boldsymbol{e}_q} H(m), \tag{26}$$

where $\mathbf{e}_q$ is the $q$-th orthonormal basis for a Euclidean space $\mathbb{R}^N$, i.e., its $q$-th element is equal to 1 and others are 0.

**Lemma 4** (Lyapunov equation). *For the convenience of the calculation of $\nabla_m H$, we define $\mathbf{b}(m) := \mathbf{B}(m)\delta\mathbf{P}$ and use Eq. (12) with **Lemma 2** to rewrite $H(m)$ as*

$$H(m) = \mathbf{b}(m)^\top \mathbf{O}(m)\mathbf{b}(m), \tag{27}$$

*with*

$$\mathbf{O}(m) = \int_0^\infty e^{\mathbf{J}^\top t} \mathbf{Q} e^{\mathbf{J}t} dt. \tag{28}$$

$\mathbf{O}(m)$ *satisfies the Lyapunov equation*

$$\mathbf{O}(m)\mathbf{J}(m) + \mathbf{O}(m)\mathbf{J}(m)^\top + \mathbf{Q}(m) = \mathbf{0}. \tag{29}$$

*Proof.* By taking the derivative of $e^{\mathbf{J}^\top t}\mathbf{Q}e^{\mathbf{J}t}$ with respect to $t$, and integrating the derivative from $t = 0$ to $t = \infty$, we have

$$\int_0^\infty \frac{d}{dt}(e^{\mathbf{J}^\top t}\mathbf{Q}e^{\mathbf{J}t})\,dt = \mathbf{O}(m)\mathbf{J}(m)^\top + \mathbf{O}(m)\mathbf{J}(m). \tag{30}$$

Using the fact that

$$e^{\mathbf{J}^\top t}\mathbf{Q}e^{\mathbf{J}t} \to \mathbf{0} \text{ for } t \to \infty, \text{ and } e^{\mathbf{J}^\top t}\mathbf{Q}e^{\mathbf{J}t} = \mathbf{Q}(m) \text{ for } t = 0.$$

We obtain the Lyapunov equation

$$\mathbf{O}(m)\mathbf{J}(m) + \mathbf{O}(m)\mathbf{J}(m)^\top + \mathbf{Q}(m) = \mathbf{0},$$

which implies $\mathbf{O}(m)$ is the unique solution of the Lyapunov equation Eq. (29). $\qquad\square$

**Lemma 5** (First order performance metric). *Substituting $H(m + \sigma\boldsymbol{\xi})$ into Eq. (27), we have*

$$H(m + \sigma\boldsymbol{\xi}) = \mathbf{b}(m + \sigma\boldsymbol{\xi})^\top \mathbf{O}(m + \sigma\boldsymbol{\xi})\mathbf{b}(m + \sigma\boldsymbol{\xi}). \tag{31}$$

*Both sides of Eq. (31) are considered as functions of a scalar $\sigma$ and are expanded in a Taylor series around $\sigma = 0$. $\boldsymbol{b}^{(1)}(m, \boldsymbol{\xi})$ and $\boldsymbol{O}^{(1)}(m, \boldsymbol{\xi})$ represent the coefficient of $\sigma$, and we have*

$$H^{(1)} = \mathbf{b}^{(1)\top}\mathbf{O}\mathbf{b} + \mathbf{b}^\top\mathbf{O}^{(1)}\mathbf{b} + \mathbf{b}^\top\mathbf{O}\mathbf{b}^{(1)}, \tag{32}$$

*where*

$$\mathbf{b}^{(1)}(m, \boldsymbol{\xi}) = \begin{bmatrix} \mathbf{0} \\ -\boldsymbol{\Psi}\mathbf{M}^{-2}\boldsymbol{v}^\omega \end{bmatrix} \tag{33}$$

*and $\boldsymbol{\Psi} = diag\{\boldsymbol{\xi}_i\}$,*

$$\mathbf{O} = \int_0^\infty e^{\mathbf{J}^\top t}\mathbf{Q}e^{\mathbf{J}t}dt, \tag{34}$$

*and* $$\mathbf{O}^{(1)} = \int_0^\infty e^{\mathbf{J}^\top t}\left(\mathbf{O}\mathbf{J}^{(1)} + \mathbf{J}^{(1)\top}\mathbf{O} + \mathbf{Q}^{(1)}\right)e^{\mathbf{J}t}dt. \tag{35}$$

*and we drop the arguments $(\sigma, \boldsymbol{\xi})$ for the convergence of simplification. Using the eigendecomposition of the matrix $\mathbf{J}$ and the Taylor series of $\mathbf{J}(m + \sigma\boldsymbol{\xi})$, $\mathbf{Q}(m + \sigma\boldsymbol{\xi})$, we obtain further*

$$\mathbf{O} = \sum_{i,j=2}^{2N} \frac{\langle \mathbf{u}_i^r, \mathbf{Q}\mathbf{u}_j^r\rangle}{\lambda_i^* + \lambda_j} \mathbf{u}_i^l\mathbf{u}_j^{l\top}, \tag{36}$$

*and*

$$\mathbf{O}^{(1)} = \sum_{i,j=2}^{2N} \frac{\langle \mathbf{u}_i^r, \left(\mathbf{O}\mathbf{J}^{(1)} + \mathbf{J}^{(1)\top}\mathbf{O} + \mathbf{Q}^{(1)}\right)\mathbf{u}_j^r\rangle}{\lambda_i^* + \lambda_j} \mathbf{u}_i^l\mathbf{u}_j^{l\top}, \tag{37}$$

*where*

$$\mathbf{J}^{(1)}(m, \boldsymbol{\xi}) = \begin{bmatrix} \mathbf{0} & \mathbf{0} \\ \boldsymbol{\Psi} K \mathbf{M}^{-2} \mathbf{L} & \boldsymbol{\Psi} \mathbf{M}^{-2} \end{bmatrix} \tag{38}$$

*and*

$$\mathbf{Q}^{(1)}(m, \boldsymbol{\xi}) = \begin{bmatrix} \mathbf{0} & \mathbf{0} \\ \mathbf{0} & \frac{1}{2} \boldsymbol{\Psi} \end{bmatrix} \tag{39}$$

*denote the coefficient of $\sigma$.*

*Proof.* First of all, for Eq. (31), we need to find expressions for $\mathbf{O}(m + \sigma \boldsymbol{\xi})$ and $\mathbf{b}(m + \sigma \boldsymbol{\xi})$. The right sides of Eq. (31) are considered as functions of a scalar $\sigma$ and are expanded in a Taylor series around $\sigma = 0$ as

$$\mathbf{b}(m + \sigma \boldsymbol{\xi}) = \mathbf{b}(m) + \mathbf{b}^{(1)}(m, \boldsymbol{\xi})\sigma + O(\sigma^2), \tag{40}$$

and

$$\mathbf{O}(m + \sigma \boldsymbol{\xi}) = \mathbf{O}(m) + \mathbf{O}^{(1)}(m, \boldsymbol{\xi})\sigma + O(\sigma^2). \tag{41}$$

By inserting Eqs. (25), (40)-(41) into Eq. (31) and comparing the coefficients in the order of $\sigma$, we obtain the first-order correction to the performance metric $H$:

$$H^{(1)}(m, \boldsymbol{\xi}) = \mathbf{b}^{(1)}(m, \boldsymbol{\xi})^\top \mathbf{O}(m)\mathbf{b}(m) + \mathbf{b}(m)^\top \mathbf{O}^{(1)}(m, \boldsymbol{\xi})\mathbf{b}(m) + \mathbf{b}(m)^\top \mathbf{O}(m)\mathbf{b}^{(1)}(m, \boldsymbol{\xi}),$$

where we use the fact that $H(m) = \mathbf{b}(m)^\top \mathbf{O}(m)\mathbf{b}(m)$.

Now, to determine $\mathbf{O}^{(1)}(m, \boldsymbol{\xi})$ we can make use of the fact that $\mathbf{O}(m + \sigma \boldsymbol{\xi})$ is also subject to the Lyapunov equation Eq. (29), which then contains the terms $\mathbf{J}(m + \sigma \boldsymbol{\xi})$ and $\mathbf{Q}(m + \sigma \boldsymbol{\xi})$:

$$\mathbf{J}(m + \sigma \boldsymbol{\xi}) = \mathbf{J}(m) + \mathbf{J}^{(1)}(m, \boldsymbol{\xi})\sigma + O(\sigma^2), \tag{42}$$

$$\text{and } \mathbf{Q}(m + \sigma \boldsymbol{\xi}) = \mathbf{Q}(m) + \mathbf{Q}^{(1)}(m, \boldsymbol{\xi})\sigma. \tag{43}$$

By substituting Eqs. (41), (42) and (43) into the original Lyapunov equation and collecting terms associated with powers of $\sigma$, we get two Lyapunov equations determining $\mathbf{O}$ and $\mathbf{O}^{(1)}$,

$$\mathbf{O}\mathbf{J} + \mathbf{J}^\top \mathbf{O} + \mathbf{Q} = \mathbf{0}, \tag{44}$$

$$\text{and } \mathbf{O}^{(1)}\mathbf{J} + \mathbf{J}^\top \mathbf{O}^{(1)} + (\mathbf{O}\mathbf{J}^{(1)} + \mathbf{J}^{(1)^\top}\mathbf{O} + \mathbf{Q}^{(1)}) = \mathbf{0}. \tag{45}$$

Note that the arguments $(\sigma, \boldsymbol{\xi})$ have been dropped in favour of readability. By using **Lemma 4**, we obtain the solutions of the two Lyapunov equations Eqs. (44) and (45), respectively,

$$\mathbf{O} = \int_0^\infty e^{\mathbf{J}^\top t} \mathbf{Q} e^{\mathbf{J}t} dt,$$

$$\text{and } \mathbf{O}^{(1)} = \int_0^\infty e^{\mathbf{J}^\top t} \left( \mathbf{O}\mathbf{J}^{(1)} + \mathbf{J}^{(1)^\top}\mathbf{O} + \mathbf{Q}^{(1)} \right) e^{\mathbf{J}t} dt.$$

Using the eigendecomposition of the matrix $\mathbf{J}$, we have

$$\mathbf{O} = \sum_{i,j=2}^{2N} \frac{\langle \mathbf{u}_i^r, \mathbf{Q}\mathbf{u}_j^r \rangle}{\lambda_i^* + \lambda_j} \mathbf{u}_i^l \mathbf{u}_j^{l\,\dagger}, \tag{46}$$

and

$$\mathbf{O}^{(1)} = \sum_{i,j=2}^{2N} \frac{\langle \mathbf{u}_i^r, \left( \mathbf{O}\mathbf{J}^{(1)} + \mathbf{J}^{(1)\top}\mathbf{O} + \mathbf{Q}^{(1)} \right) \mathbf{u}_j^r \rangle}{\lambda_i^* + \lambda_j} \mathbf{u}_i^l \mathbf{u}_j^{l\,\dagger}. \tag{47}$$

In the rest of our proof, we compute the coefficients of the Taylor expansion in Eqs. (40),(42) and (43). Recall the scalar series expansion of $1/(m_i + \sigma\xi_i)$ around $\sigma = 0$:

$$\frac{1}{m_i + \sigma\xi_i} = \frac{1}{m_i} - \frac{\sigma\xi_i}{m_i^2} + O(\sigma^2). \tag{48}$$

We take the shorthand $\mathbf{\Psi} = diag\{\xi_i\}$ and use Eq. (48) to directly obtain the following terms up to $O(\sigma^2)$:

$$\mathbf{b}^{(1)}(m, \boldsymbol{\xi}) = \begin{bmatrix} \mathbf{0} \\ -\mathbf{\Psi}\mathbf{M}^{-2}\boldsymbol{v}^\omega \end{bmatrix}, \tag{49}$$

$$\mathbf{J}^{(1)}(m, \boldsymbol{\xi}) = \begin{bmatrix} \mathbf{0} & \mathbf{0} \\ \mathbf{\Psi}K\mathbf{M}^{-2}\mathbf{L} & \mathbf{\Psi}\mathbf{M}^{-2} \end{bmatrix}, \tag{50}$$

and

$$\mathbf{Q}^{(1)}(m, \boldsymbol{\xi}) = \begin{bmatrix} \mathbf{0} & \mathbf{0} \\ \mathbf{0} & \frac{1}{2}\mathbf{\Psi} \end{bmatrix}. \tag{51}$$

$\square$

**Theorem 1** (Inertia gradient). *Selecting $\boldsymbol{\xi} = \mathbf{e}_q$, the q-th component of the gradient $\nabla_m H$ is*

$$(\nabla_m H)_q = \mathbf{b}^{(1)\top}\mathbf{O}\mathbf{b} + \mathbf{b}^\top\mathbf{O}^{(1)}\mathbf{b} + \mathbf{b}^\top\mathbf{O}\mathbf{b}^{(1)}. \tag{52}$$

*Proof.* Substituting Eq. (26) into Eq.(24) of **Lemma 3**, we have

$$(\nabla_m H)_q = H^{(1)}(m, \mathbf{e}_q). \tag{53}$$

Substituting Eq. (53) into Eq. (32) of **Lemma 5**, we obtain

$$(\nabla_m H)_q = \mathbf{b}^{(1)\top}\mathbf{O}\mathbf{b} + \mathbf{b}^\top\mathbf{O}^{(1)}\mathbf{b} + \mathbf{b}^\top\mathbf{O}\mathbf{b}^{(1)}. \tag{54}$$

$\square$

Up to now, we have evaluated $(\nabla_m H)_q$ based on **Lemma 3-5** and **Theorem 1**. To clearly exhibit our results, we show the proofs of **Lemma 3-5** and **Theorem 1** by following the general framework of [31]. By using eigendecomposition of the matrix $\mathbf{J}$, we extend the expressions of $\mathbf{O}$ and $\mathbf{O}^{(1)}$ in favour of simulation. At the beginning of this section, in Fig. 3(a), three cases for perturbations were introduced (phase, frequency or joint perturbation). Varying the inertia $m$ in the interval $[0.5; 10]$, we complement the analysis of the inertia effect with our analytic results for $(\nabla_m H)_q$ in Fig. 3(b). For case (i), $(\nabla_m H)_q$ is close to 0, i.e., the variation of the inertia does not affect the transient performance of the system. However, for the cases of (ii) and (iii), we conclude that $(\nabla_m H)_q > 0$, i.e., $H$ monotonically increases with the variations of $m$ and the system becomes unstable with the increases of the inertia. Therefore, these analytical results from Fig. 3(b) are consistent with Fig. 3(a).

## IV. Local coherency performance metric

We have introduced the coherency performance metric $H$ which measures the stability of the whole system given a delta perturbation $\delta\mathbf{P} = [v^\theta, v^\omega]^\top$ and have analyzed the different sensitivity in the phase and frequency directions with respect to the inertia in the strong-coupling regime with $K = 1.0$. Instead of the global performance metric in a strongly-coupled regime, we focus now on a local definition that quantifies the transient performance at each node separately and extends the analysis to a weakly-coupled regime.

For perturbations $\delta\mathbf{P}_q = [0, \ldots, v_q^\theta, \ldots, 0, 0, \ldots, v_q^\omega, \ldots, 0]^\top$ localised at the $q$-th node, we define the local metric $H_k(\delta\mathbf{P}_q)$ to measure the energy variations of the $k$-th node as

$$H_{kq} := H_k(\delta\mathbf{P}_q) = \int_0^\infty \left\{ \sum_{j=1}^n a_{kj}(\delta\theta_k(t) - \delta\theta_j(t))^2 + \frac{1}{2} m_k \delta\omega_k(t)^2 \right\} dt, \tag{55}$$

with $k \neq q$ and $k, q = 1, \cdots, N$. The global metric $H$ in Eq. (15) is retrieved by summing the local ones across the influenced nodes, i.e. $H = \sum_{k=1}^N H_k$.

**Lemma 6** (Generalized coherency performance metric). *Using the solution of* $\mathbf{x}$, *we obtain the analytic solution of* $H_{kq}$ *is*

$$H_{kq} = -\mathbf{e}_k^\top \sum_{i,j=2}^{2N} \langle \mathbf{u}_i^l, \mathbf{B}\delta\mathbf{P}_q \rangle \left\{ \begin{bmatrix} \mathbf{I} & \mathbf{I} \end{bmatrix} \frac{diag\{\mathbf{u}_i^r\}}{\lambda_i + \lambda_j} \begin{bmatrix} \tilde{\mathbf{L}} - \mathbf{A} & \mathbf{0} \\ \mathbf{0} & \frac{1}{2}\mathbf{M} \end{bmatrix} - \begin{bmatrix} \mathbf{A} & \mathbf{0} \end{bmatrix} \frac{diag\{\mathbf{u}_i^r\}}{\lambda_i + \lambda_j} \right\} \langle \mathbf{u}_j^l, \mathbf{B}\delta\mathbf{P}_q \rangle \mathbf{u}_j^r. \tag{56}$$

*Proof.* For convenience of computation, we rewrite Eq. (55) as

$$H_{kq} = \int_0^\infty \mathbf{e}_k^\top \left\{ \delta\mathbf{\Theta}(\tilde{\mathbf{L}} - \mathbf{A})\delta\boldsymbol{\theta} + \frac{1}{2}\delta\mathbf{\Omega}\mathbf{M}\delta\boldsymbol{\omega} + \mathbf{A}\delta\mathbf{\Theta}\delta\boldsymbol{\theta} \right\} dt, \tag{57}$$

where $\delta\mathbf{\Theta} = diag\{\delta\theta_i\} \in \mathbb{R}^{N \times N}$ and $\delta\mathbf{\Omega} = diag\{\delta\omega_i\} \in \mathbb{R}^{N \times N}$ are the diagonal phase-difference matrix and diagonal frequency-displacement matrix, respectively. We also diagonalize the corresponding state matrix as $\mathbf{X} = diag\{x_i\} \in \mathbb{R}^{2N \times 2N}$ and rewrite Eq. (57) as

$$H_{kq} = \int_0^\infty \mathbf{e}_k^\top \left\{ \begin{bmatrix} \mathbf{I} & \mathbf{I} \end{bmatrix} \mathbf{X} \begin{bmatrix} \tilde{\mathbf{L}} - \mathbf{A} & \mathbf{0} \\ \mathbf{0} & \frac{1}{2}\mathbf{M} \end{bmatrix} \mathbf{x} + \begin{bmatrix} \mathbf{A} & \mathbf{0} \end{bmatrix} \mathbf{X}\mathbf{x} \right\} dt. \tag{58}$$

Substituting the solution Eq. (14) of $\mathbf{x}$ into the diagonal state matrix, we have

$$\mathbf{X} = \sum_{i=2}^{2N} e^{\lambda_i t} \langle \mathbf{u}_i^l, \mathbf{B}\delta\mathbf{P}_q \rangle diag\{\mathbf{u}_i^r\}, \tag{59}$$

where for the vector $\mathbf{u}_i^r$, $diag\{\mathbf{u}_i^r\}$ is a diagonal matrix. Substituting Eq. (59) into Eq. (58) finally yields Eq. (56). $\square$

We have already obtained the analytic solution of $H_{kq}$ expressed in Eq. (56) and contrast it with numerical simulations of Eq. (55). Using again the same setting as in Fig. 2, we perturb the frequency $\omega_q$ and phase $\theta_q$ of node $q$, $q = 1, \cdots, N$. This corresponds to case (iii) in Fig. 3. We evaluate each of the other nodes' response and get a matrix $\mathbf{H}$ with $N \times N$ elements, where the diagonal elements of $\mathbf{H}$ are 0, and the off-diagonal elements are the energy variations of node $k$, with $k \neq q$. For illustration purpose only, we depict the block ($15 \times 15$) of $\mathbf{H}$ in Fig. 4. The

x-axis denotes the location of perturbations, the y-axis denotes the perturbed nodes and the color reflects the values of the corresponding energy variations.

For $K = 0.5$, we obtain the analytic $\mathbf{H}^a$ and numerical solutions $\mathbf{H}^s$ of $\mathbf{H}$ in Fig. 4(a) and (e), respectively. The results are close upon visual inspection. However, in order to quantify the similarity between the analytic and numerical solutions of $\mathbf{H}$, we use the Pearson correlation coefficient defined as

$$r = \frac{\sum_{k=1}^{N}\sum_{q=1}^{N}(\mathbf{H}_{kq}^a - \bar{\mathbf{H}}^a)(\mathbf{H}_{kq}^s - \bar{\mathbf{H}}^s)}{\sqrt{\sum_{k=1}^{N}\sum_{q=1}^{N}(\mathbf{H}_{kq}^a - \bar{\mathbf{H}}^a)^2}\sqrt{\sum_{k=1}^{N}\sum_{q=1}^{N}(\mathbf{H}_{kq}^s - \bar{\mathbf{H}}^s)^2}}, \tag{60}$$

where

$$\bar{\mathbf{H}}^a = \frac{1}{N^2}\sum_{k=1}^{N}\sum_{q=1}^{N}H_{kq}^a, \text{ and } \bar{\mathbf{H}}^s = \frac{1}{N^2}\sum_{k=1}^{N}\sum_{q=1}^{N}H_{kq}^s,$$

are the averages over the entries in $\mathbf{H}^a$ and $\mathbf{H}^s$, respectively. Indeed, for $K = 0.5$, the Pearson correlation coefficient is $r = 0.9999$.

We also numerically calculate the local metric for weak coupling strengths. For sufficiently low $K$, the system exhibits large transients even after small perturbations and some nodes do not return to the synchronous regime, indicating multistability. Hence, our linear approximation of the dynamics breaks down hand in hand with a loss of coherence in the final state. In this case, the local metrics could be much larger as shown for $K = 0.04$ in Fig. 4(b). With the increase of the coupling strength $K$, the synchronization coherence increases, local metrics decrease correspondingly in Fig. 4(c)-(e), and the order parameter $R$ increases as shown in Fig. 4(f). Meanwhile, the similarity between the analytical solutions (obtained for strong coupling strength $K = 0.5$) and the numerical ones (for weak coupling strengths) increases as shown in Fig. 4(g). The local energy variation reflects the sensitivity of the nodes. With the decrease of $K$, the sensitivity increases with the increases of the local energy variation. For example, for $K = 0.04$ in Fig. 4(b), the 5-th node is easily perturbed by other nodes. This could be due to multiple reasons and nodes' local topological properties could be the main reason. To investigate the influence of the network topology, below the local performance is evaluated for different network motifs.

As we have seen, the local performance $H_{kq}$ is largely determined by the underlying network structure. To get a more systematic picture, we determine $\mathbf{H}^a$ and $\mathbf{H}^s$ for specific motifs. We take three motifs ①-③ shown in Fig. 5 with one consumer (the 1st node with $\omega_1 = -1$) and two generators (the 2nd and 3rd nodes with $\omega_2 = \omega_3 = 0.5$). As an illustration, we perturb both the frequency $\omega_1$ and phase $\theta_1$ in the three motifs, show the analytical and numerical solutions of the local metrics on the 1st node (shown in the second column) and on the 2nd node (shown in the third column) in Fig. 5. Here, we display the standard deviation (in red and blue shaded area) and mean values (red and blue curve) of $H_{11}$, $H_{21}$ (simulation and analytic).

Our results exhibit casual influence between each pair of nodes, and indicate that for the local linear response indicate, given fixed perturbation, nodes are subject to a certain topological vulnerability. The network topology determines highly responsive nodes as well as critical locations. The local metrics are influenced by many factors, especially by an interplay of their topology and the kind of perturbation. Even given the topology but varying the spatial distribution of generators or consumers, as shown in ① and ③ of Fig. 5, the resulting metrics vary from, e.g., the maximal values and nodes' casual responses. Perturbations can also affect the results of local metrics. We vary both the value of perturbation $\delta\theta_1$ of phase and $\delta\omega_1$ of frequency of the 1st node from -0.5 to 0.5, and calculate the local metric of $H_{11}$, shown in the last column of Fig. 5.

## V. Conclusion

The theoretical interest in the Kuramoto model with inertia is due to its diverse collective behavior, including chaotic dynamics at intermediate coupling strengths and network sizes. It is also practically useful to systems functioning

of, e.g., power transmission grids. In this work, we have exploited the coherency performance metric to investigate the influence of the inertia on the system stability. Especially, we have first formulated the analytical expression of the metric as a function of topological and dynamical properties given small perturbations. We have also derived a gradient algorithm to further quantify the derivation of the metric with respect to the inertia, and have shown that the values of the metric generally decrease with the decrease of the inertia. We have additionally generalized the global performance metric to the local one, have analyzed the causal effects of the stability influences, and have shown that the analytical results can be further extended to the case of weak coupling. The local performance metric quantifies the pairwise casual influence between any two nodes and could easily reveal vulnerable nodes. However, the current framework is based on small perturbations and on coherent states. It is also straight-forward to extend the analysis to incoherent and chaotic states [34]. Furthermore, it is interesting to extend the theoretical framework for large perturbations and to analyze the placement of the power on the system stability. Beyond impulsive perturbations, the linear response of synchronisation in complex networks to sequences of perturbations recently have become a focus [33] and it is an interesting avenue for future research to generalize our results to time-dependent perturbations. Additional to the three motifs, it is also quite interesting to extend the investigation to a detour structure [39], other small motifs [40], and trees [41].

## VI.    Conflicts of interest

The authors have no conflicts of interest regarding the publication of this paper.
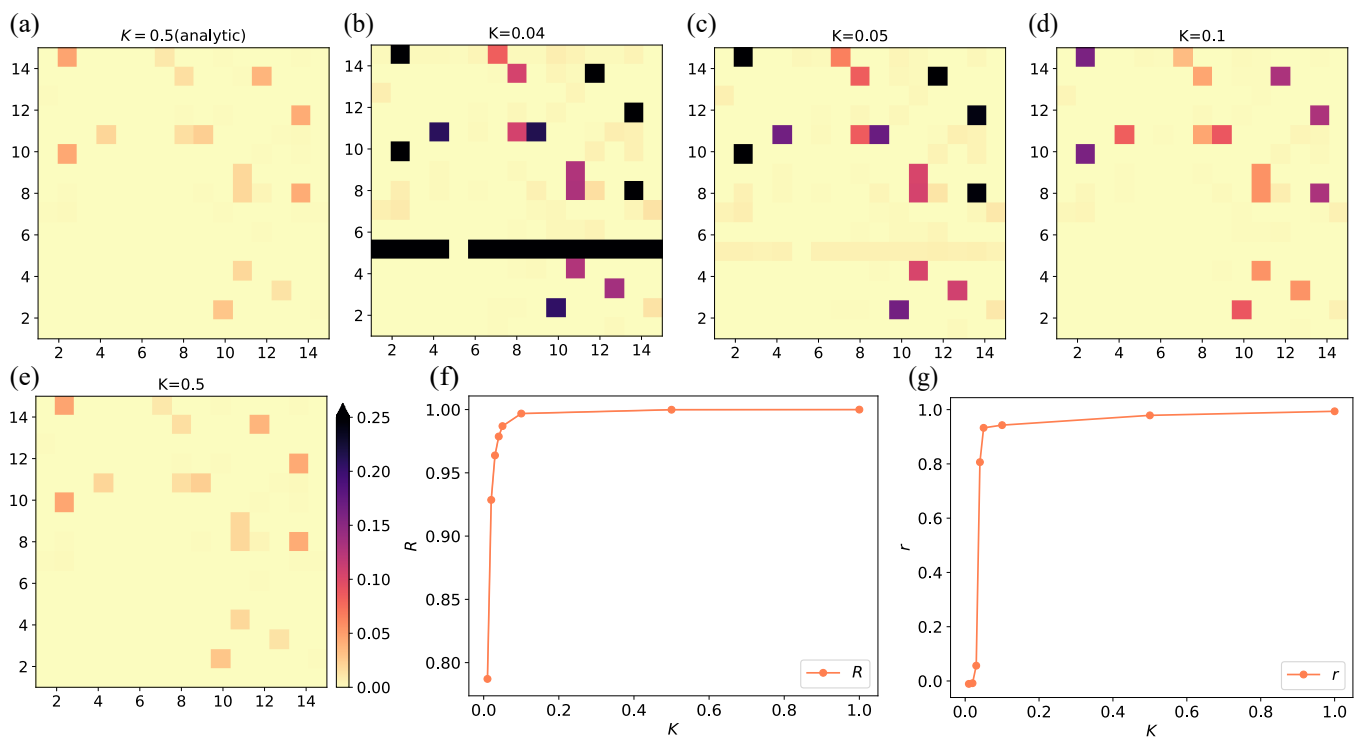


FIG. 4: (a) When the coupling strength $K = 1.0$, the figures of analytic and numerical solutions of $\mathbf{H}$, where we only show part $(15 \times 15)$ of the solutions, and $m = 1.0$. (b)-(e) Figures of coherency performance metric $\mathbf{H}$ with respect to different coupling strength $K$, where we perturb both the frequency $\omega$ and the phase $\theta$ of each node in turn, only part $(15 \times 15)$ of the numerical solutions $\mathbf{H}$ are shown. $K$ is from 0.04 to 0.5, and $m = 1.0$. (f) Figure of order parameter $R$ with respect to the coupling strength $K$, where $K$ is 0.01 from to 1.0, and the inertia $m = 1.0$. (g) Figure of Pearson correlation coefficient $r$ with respect to different coupling strength $K$, where $K$ is 0.01 from to 1.0, and the inertia $m = 1.0$. Here, $N_1 = 30$ and $N_2 = 70$.

# VII.   ACKNOWLEDGEMENTS

[1] Steven H Strogatz. From kuramoto to crawford: exploring the onset of synchronization in populations of coupled oscillators. *Physica D: Nonlinear Phenomena*, 143(1-4):1–20, 2000.

[2] Juan A Acebrón, Luis L Bonilla, Conrad J Pérez Vicente, Félix Ritort, and Renato Spigler. The kuramoto model: A simple paradigm for synchronization phenomena. *Reviews of modern physics*, 77(1):137, 2005.

[3] Alex Arenas, Albert Díaz-Guilera, Jurgen Kurths, Yamir Moreno, and Changsong Zhou. Synchronization in complex networks. *Physics reports*, 469(3):93–153, 2008.

[4] Francisco A Rodrigues, Thomas K DM Peron, Peng Ji, and Jürgen Kurths. The kuramoto model in complex networks. *Physics Reports*, 610:1–98, 2016.
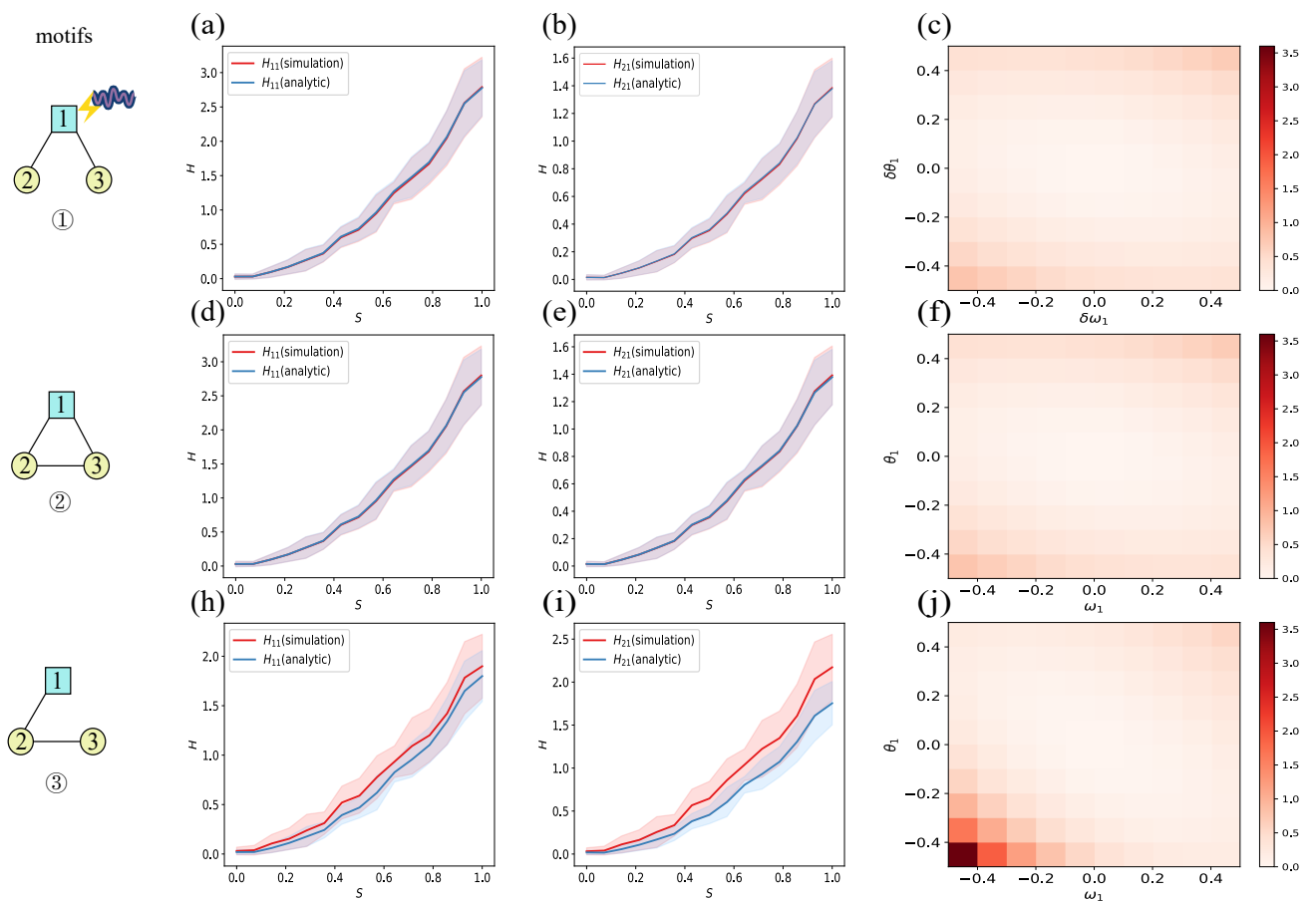


FIG. 5: ①-③ are three motifs. For the 1st node, the motifs ① and ② are symmetric connections, while the motif ③ is asymmetric connections. (a)-(b), (d)-(e), and (h)-(i) When we perturb the 1st node, we obtain the responds of the 1st and the 2nd node. (c), (f), and (j) The variations of $H_{11}$ when we variate both the phase difference and the frequency displacement of the 1st node from -0.5 to 0.5. The parameters of (a)-(j) are $K = 1.0$, $m_i = 1.0$, $P_1 = -1.0$, and $P_2 = P_3 = 0.5$.

[5] Per Sebastian Skardal, Juan G Restrepo, and Edward Ott. Frequency assortativity can induce chaos in oscillator networks. *Physical Review E*, 91(6):060902, 2015.

[6] Paul So and Ernest Barreto. Generating macroscopic chaos in a network of globally coupled phase oscillators. *Chaos: An Interdisciplinary Journal of Nonlinear Science*, 21(3):033127, 2011.

[7] Maxim Komarov and Arkady Pikovsky. Dynamics of multifrequency oscillator communities. *Physical review letters*, 110(13):134101, 2013.

[8] Oleksandr V Popovych, Yuri L Maistrenko, and Peter A Tass. Phase chaos in coupled oscillators. *Physical Review E*, 71(6):065201, 2005.

[9] Yuri L Maistrenko, Oleksandr V Popovych, and Peter A Tass. Chaotic attractor in the kuramoto model. *International Journal of Bifurcation and Chaos*, 15(11):3457–3466, 2005.

[10] Matthias Wolfrum, Oleh E Omelchenko, Serhiy Yanchuk, and Yuri L Maistrenko. Spectral properties of chimera states. *Chaos: An Interdisciplinary Journal of Nonlinear Science*, 21(1):013112, 2011.

[11] Simona Olmi, Adrian Navas, Stefano Boccaletti, and Alessandro Torcini. Hysteretic transitions in the kuramoto model with inertia. *Physical Review E*, 90(4):042905, 2014.

[12] JA Acebrón, LL Bonilla, and R Spigler. Synchronization in populations of globally coupled oscillators with inertial effects. *Physical Review E*, 62(3):3437, 2000.

[13] Seung-Yeal Ha, Se Eun Noh, and Jinyeong Park. Interplay of inertia and heterogeneous dynamics in an ensemble of kuramoto oscillators. *Analysis and Applications*, 15(06):837–861, 2017.

[14] Young-Pil Choi, Seung-Yeal Ha, and Javier Morales. Emergent dynamics of the kuramoto ensemble under the effect of inertia. *arXiv preprint arXiv:1707.07164*, 2017.

[15] Chun-Hsiung Hsia, Chang-Yeol Jung, and Bongsuk Kwon. On the synchronization theory of kuramoto oscillators under the effect of inertia. *Journal of Differential Equations*, 267(2):742–775, 2019.

[16] Julien Barre and David Métivier. Bifurcations and singularities for coupled oscillators with inertia and frustration. *Physical review letters*, 117(21):214102, 2016.

[17] Hisa-Aki Tanaka, Allan J Lichtenberg, and Shin'ichi Oishi. First order phase transition resulting from finite inertia in coupled oscillator systems. *Physical review letters*, 78(11):2104, 1997.

[18] Yuri Maistrenko, Serhiy Brezetsky, Patrycja Jaros, Roman Levchenko, and Tomasz Kapitaniak. Smallest chimera states. *Physical Review E*, 95(1):010203, 2017.

[19] Frank Hellmann, Paul Schultz, Patrycja Jaros, Roman Levchenko, Tomasz Kapitaniak, Jürgen Kurths, and Yuri Maistrenko. Network-induced multistability through lossy coupling and exotic solitary states. *Nature Communications*, 11(1):1–9, 2020.

[20] Halgurd Taher, Simona Olmi, and Eckehard Schöll. Enhancing power grid synchronization and stability through time-delayed feedback control. *Physical Review E*, 100(6):062306, 2019.

[21] Martin Rohden, Andreas Sorge, Marc Timme, and Dirk Witthaut. Self-organized synchronization in decentralized power grids. *Physical review letters*, 109(6):064101, 2012.

[22] Fabio Pasqualetti, Florian Dörfler, and Francesco Bullo. Attack detection and identification in cyber-physical systems. *IEEE transactions on automatic control*, 58(11):2715–2729, 2013.

[23] Keren Li, Shen Ma, Haihong Li, and Junzhong Yang. Transition to synchronization in a kuramoto model with the first-and second-order interaction terms. *Physical Review E*, 89(3):032917, 2014.

[24] Louis M Pecora and Thomas L Carroll. Master stability functions for synchronized coupled systems. *Physical review letters*, 80(10):2109, 1998.

[25] Peter J Menck, Jobst Heitzig, Norbert Marwan, and Jürgen Kurths. How basin stability complements the linear-stability paradigm. *Nature physics*, 9(2):89, 2013.

[26] Malte Schröder, Marc Timme, and Dirk Witthaut. A universal order parameter for synchrony in networks of limit cycle oscillators. *Chaos: An Interdisciplinary Journal of Nonlinear Science*, 27(7):073119, jul 2017.

[27] Per Sebastian Skardal, Dane Taylor, and Jie Sun. Optimal synchronization of complex networks. *Physical Review Letters*, 113(14):144101, October 2014.

[28] C. Grabow, S. M. Hill, S. Grosskinsky, and M. Timme. Do small worlds synchronize fastest? *EPL (Europhysics Letters)*, 90(4):48002, 2010.

[29] David J Jörg, Luis G Morelli, Saúl Ares, and Frank Jülicher. Synchronization dynamics in the presence of coupling delays and phase shifts. *Physical Review Letters*, 112(17):174101, May 2014.

[30] Paul Schultz, Frank Hellmann, Kevin N. Webster, and Jürgen Kurths. Bounding the first exit from the basin: Independence times and finite-time basin stability. *Chaos: An Interdisciplinary Journal of Nonlinear Science*, 28(4):043102, apr 2018.

[31] Bala Kameshwar Poolla, Saverio Bolognani, and Florian Dörfler. Placing Rotational Inertia in Power Grids. *Proceedings of the American Control Conference*, 2016-July:2314–2320, oct 2016.

[32] M Tyloo, T Coletta, and Ph Jacquod. Robustness of Synchrony in Complex Networks and Generalized Kirchhoff Indices. *Physical Review Letters*, 120(8):084101, February 2018.

[33] Anton Plietzsch, Sabine Auer, Jürgen Kurths, and Frank Hellmann. A generalized linear response theory of complex networks with an application to renewable fluctuations in microgrids. *arXiv preprint arXiv:1903.09585*, 2019.

[34] Johnatan Aljadeff, Merav Stern, and Tatyana Sharpee. Transition to chaos in random networks with cell-type-specific connectivity. *Physical Review Letters*, 114(8):088101, February 2015.

[35] Simona Olmi. Chimera states in coupled kuramoto oscillators with inertia. *Chaos: An Interdisciplinary Journal of Nonlinear Science*, 25(12):123125, 2015.

[36] Arthur R Bergen and David J Hill. A structure preserving model for power system stability analysis. *IEEE Transactions on Power Apparatus and Systems*, (1):25–35, 1981.

[37] Izrail Moiseevich Gelfand and Georgii Evgenevich Shilov. *Generalized functions, Vol. 4: applications of harmonic analysis*. Academic Press, 1964.

[38] Edwin Hewitt and Karl Stromberg. *Real and abstract analysis: a modern treatment of the theory of functions of a real variable*. Springer-Verlag, 2013.

[39] Paul Schultz, Jobst Heitzig, and Jürgen Kurths. Detours around basin stability in power networks. *New Journal of Physics*, 16(12):125001, 2014.

[40] Peng Ji and Jürgen Kurths. Basin stability of the kuramoto-like model in small networks. *The European Physical Journal Special Topics*, 223(12):2483–2491, 2014.

[41] Jan Nitzbon, Paul Schultz, Jobst Heitzig, Jürgen Kurths, and Frank Hellmann. Deciphering the imprint of topology on nonlinear dynamical network stability. *New Journal of Physics*, 19(3):033029, 2017.